Supporting Information for "Retreat of Thwaites Glacier Triggered by its Neighbours"

Matt Trevers[1], Stephen L. Cornford[1], Antony J. Payne[2], Edward Gasson[3], Suzanne Bevan[4]

[1]Centre for Polar Observation and Modelling, School of Geographical Sciences, University of Bristol, Bristol, UK

[2]School of Environmental Sciences, University of Liverpool, Liverpool, UK

[3]Centre for Geography and Environmental Sciences, University of Exeter, Cornwall, UK

[4]Department of Geography, Faculty of Science and Engineering, Swansea University, Swansea, UK

Contents of this file

Additional Supporting Information (Files uploaded separately)

1. Information and Captions for Movies S1 to S8

Corresponding author: Matt Trevers, matt.trevers@bristol.ac.uk

S1. Model Initialisation

We initialised a modern-day configuration of the Amundsen Sea Embayment (ASE) to produce smooth and consistent fields of basal friction coefficient C, ice stiffening factor ϕ and a relaxed ice geometry. This was achieved through an iterative procedure following Bevan et al. (2023) which alternates model inversions to produce optimised fields of C and ϕ with relaxation cycles in which we allowed the surface geometry to evolve. We applied the most recently calculated fields of C and ϕ during each relaxation cycle, and the updated surface geometry was applied in the next iteration of the inverse problem. The initial ice thickness came from BedMachine v3 (Morlighem, 2022).

Fields of C and ϕ were estimated by solving an inverse problem. This method is described in detail in Cornford et al. (2013). In short, smooth fields of $C(x, y)$ and $\phi(x, y)$ are chosen that minimise the misfit between modelled and observed ice flow speeds. The observed flow speed came from (Mouginot et al., 2019). Where velocity observations are available we set as the initial guess at C,

$$C_0 = \frac{\phi_i g h \left|\nabla s\right|}{\left|\boldsymbol{u}_o\right| + 1}, \tag{S.1}$$

elsewhere and outside of the ASE basin boundary we set $C_0 = 10^5$. We initially set $\phi_0 = 1$. A nonlinear conjugate gradient method was applied to find a minimum of an objective function composed of the velocity misfit function and penalty functions for $C(x, y)$ and $\phi(x, y)$. The penalty functions act to limit the magnitude of spatial gradients of $C(x, y)$ and $\phi(x, y)$, with the Tikhonov coefficients determining the relative weightings of spatial gradients of $C(x, y)$ and $\phi(x, y)$ within the objective function. The inclusion of penalty functions in the objective function serves two purposes. Firstly, without it, the inverse problem would be under-determined, that is we would be seeking values of two unknown and unconstrained fields with only one field of input data. Secondly, it limits overfitting to small changes and noise in the observed velocity. Without the penalty functions the problem would be ill-conditioned.

During the relaxation cycle, we prohibited thinning or thickening for floating ice by calculating an additional basal mass balance which opposed any thickness change. Over grounded ice we applied the mean surface mass balance from 1980 to 2021 from the MAR regional climate model (Agosta et al., 2019), from which the observed rate of thickness change from Smith et al. (2020) was subtracted. This follows a method introduced by van den Akker et al. (2023) which is intended to optimise agreement with modern observed thickening/thinning rates in the final relaxed state once the observed thickness change rate component is removed from the applied surface mass balance.

The initialisation procedure was run for 50 years. The inverse problem was solved before the first timestep of the relaxation, and then again at 10 year intervals. During both the inversion and the relaxation cycles, a linear viscous sliding law was applied:

$$\boldsymbol{\tau}_{b,l} = -C_l \boldsymbol{u}_b. \tag{S.2}$$

The units and magnitude of C_l in Equation SS.2 differ from those of the Regularised law (Equation 1). Following the initialisation procedure, we therefore calculate C by equating $\boldsymbol{\tau}_{b,r} = \boldsymbol{\tau}_{b,l}$, taking the final modelled velocity at the end of the initialisation as $\boldsymbol{u}_b$.

Figure S1 shows the state at the end of the initialisation and Figure S2 shows the model state following 1 year of a forwards model run initialised from the relaxed model state. Figures S3e and S3f show the basal shear stress $\boldsymbol{\tau}_b$ (independent of sliding law) and ice stiffening factor ϕ produced by the initialisation procedure.

S2. Thermal Spin-up

The three dimensional temperature field used in this study was derived from a thermal spin-up using the BISICLES ice sheet model. The spin-up was carried out for the whole Antarctic Ice Sheet.

Initially an inverse problem was solved to generate a realistic velocity structure for the ice sheet using the observed velocities from (Mouginot et al., 2019). Note that unlike in Section S1, we simply performed a single model inversion rather than carrying out the full iterative procedure.

The spin-up was carried out for 100,000 years at a resolution of 8 km across the full ice sheet. The ice thickness was held constant throughout the spin-up. The ice column was divided into 24 vertical layers, with increasing vertical resolution towards the bed. The mean of monthly surface temperatures from 1980 to 2021 from the MAR regional climate model (Agosta et al., 2019) provided the surface temperature boundary condition. The mean geothermal heat flow dataset from Burton-Johnson et al. (2020) provided the basal boundary condition. This dataset was compiled as a mean of five products produced by different methods.

Following the spin-up, the temperature field for the ASE domain was extracted directly from the full Antarctic field. Figure S3d shows the depth averaged temperature field within the ASE.

S3. Ice Shelf Melt Rate

A synthetic ice shelf basal melt rate was applied in the experiments in this study. We used a very simple depth-dependent parameterisation in which the melt rate varied linearly from 1 m/year as sea level to some maximum melt rate at a depth of 1000 m, remaining constant with depth thereafter. i.e.,

$$\dot{m} = 1 + (\dot{m}_{max} - 1)\,\frac{\min\left[d, 1000\right]}{1000}, \tag{S.3}$$

where $\dot{m}$ is the melt rate (defined such that positive $\dot{m}$ means removal of ice) and d is the ice shelf draft. We maintain the 1 m/year melt rate at sea level to remove thin floating ice.

The interbasin interaction experiments described in Section 2.1 use $\dot{m}_{max} = 250$ m/year. This is sufficiently large to trigger retreat while also remaining within a plausible range for a future warming scenario. It initially produced 272 Gt/year total melt from TGIS and 569 Gt/year from PIIS. While the synthesised total melt was significantly higher than observed melt of up to 100 Gt/year for both PIIS and TGIS (Rignot et al., 2013; Shean et al., 2019), melt rates of up to 250 m/year near the grounding line are consistent with both ocean models and observations (Shean et al., 2019; Holland et al., 2023).

The first group of enhanced forcing experiments described in Section 2.2 also use this depth-dependent parameterisation, but taking different values of $\dot{m}_{max}$ up to 2000 m/year.

Melting was applied only to the underside of floating ice. Masks were used to selectively apply melt either individually to the PIG, TG or CD basins or to combinations of these basins. Basin extents were provided by Mouginot et al. (2017). Melting was confined to the selected basins even where grounding lines retreated beyond basin boundaries, and to cells with direct ocean connectivity.

S4. Buttressing Number Calculation

The strength of ice shelf buttressing can be evaluated using the buttressing number, θ_n. We follow the formulation of Gudmundsson et al. (2023) which we repeat here for convenience. The buttressing number is calculated as the ratio of the resistive horizontal stress measured normal to the grounding line to the resistive stress in the absence of an ice shelf,

$$\theta_n = \frac{R_n}{R_0}, \tag{S.4}$$

where R_n is the normal component of the resistive stress vector measured across the grounding line,

$$R_n = \hat{\boldsymbol{n}}_{nl}^T \cdot \boldsymbol{R}\hat{\boldsymbol{n}}_{nl}. \tag{S.5}$$

$\hat{\boldsymbol{n}}_{nl} = [n_x \ n_y]^T$ is the unit vector normal to the grounding line and $\boldsymbol{R}$ is the resistive stress vector,

$$\boldsymbol{R} = \begin{pmatrix} 2\tau_{xx} + \tau_{yy} & \tau_{xy} \\ \tau_{xy} & \tau_{xx} + 2\tau_{yy}, \end{pmatrix} \tag{S.6}$$

resulting in

$$R_n = n_x^2 \left(2\tau_{xx} + \tau_{yy}\right) + 2n_x n_y \tau_{xy} + n_y^2 \left(\tau_{xx} + 2\tau_{yy}\right). \tag{S.7}$$

R_0 is the normal component of the resisitive horizontal stress in the absence of an ice shelf,

$$R_0 = \frac{1}{2}\rho_i \left(1 - \rho_i/\rho_w\right) gh, \tag{S.8}$$

where $\rho_i = 917$ kg m^{-1} and $\rho_w = 1027$ kg m^{-1} are the ice and ocean densities respectively, $g = 9.81$ m s^{-2} is the gravitational acceleration and h is the ice thickness.

An unbuttressed or exposed grounding line will have $R_n = R_0$, therefore by definition $\theta_n = 1$. The ice shelf provides buttressing where $\theta_n < 1$, and *anti-buttressing* where $\theta_n > 1$, i.e. the presence of the shelf acts to increase tension at the grounding line. Where $\theta_n < 0$ the ice shelf provides *super-buttressing*, i.e. the buttressing strength is such that ice at the grounding line is under compression.

Figures S1 to S8

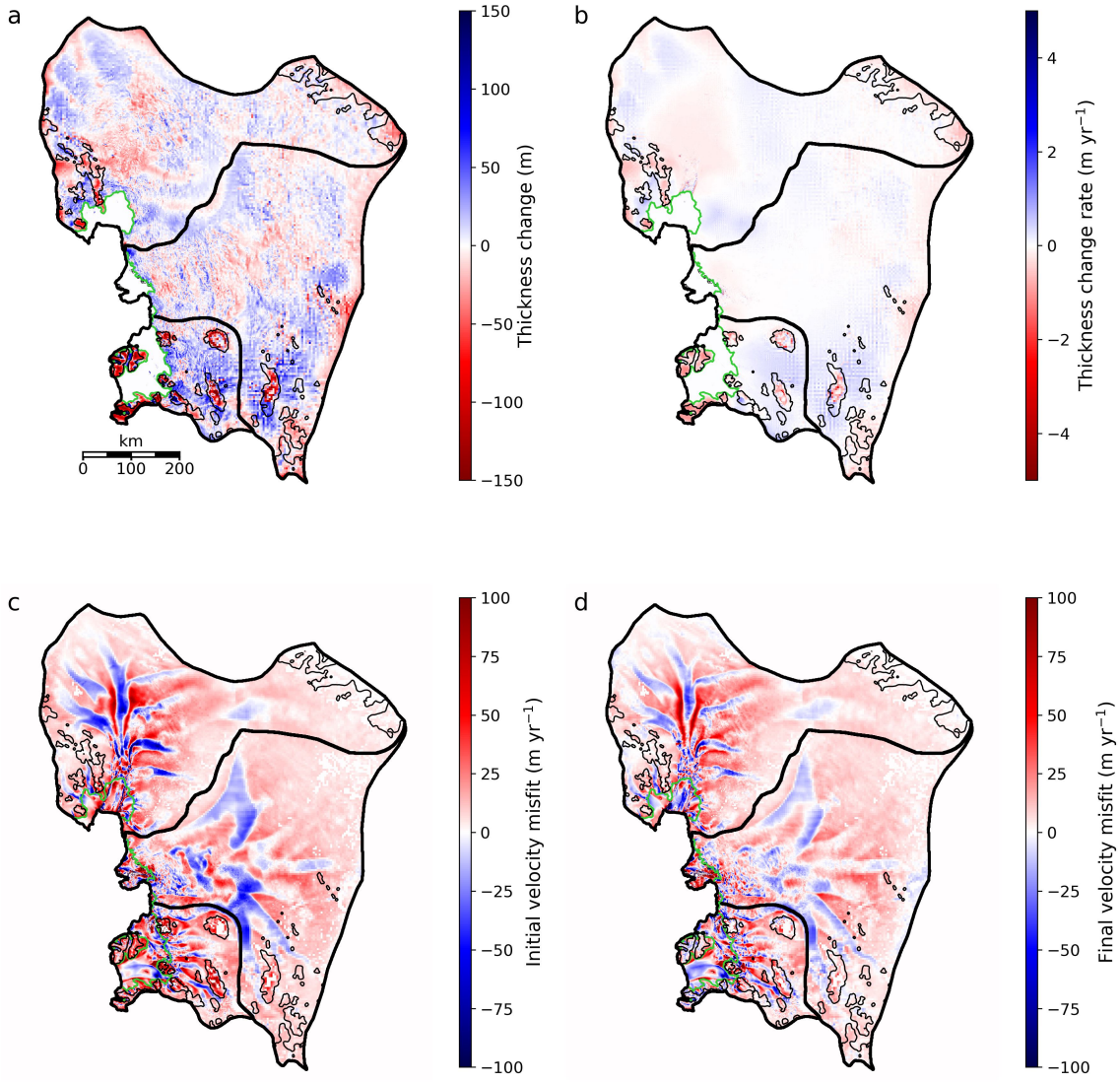

Figure S1. Initial state following the 50 year initialisation procedure. (a) Total thickness change from the original ice thickness. (b) Rate of thickness change after 50 years in the final relaxation iteration. (c) Initial ice velocity misfit. (d) Final ice velocity misfit. Thick black lines show the basin boundaries and ice extent while thin black lines show the sea level contour of bed depth. Grounding lines are marked by green lines.

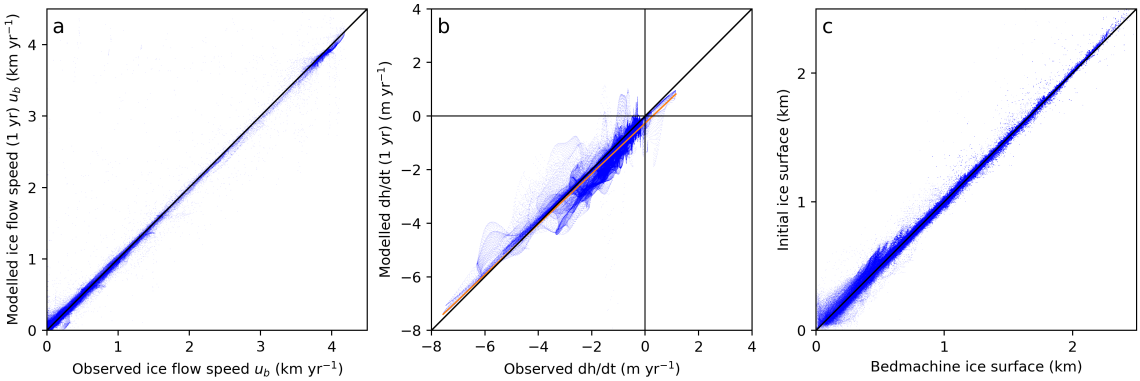

Figure S2. Model state following the first year of a forwards run started from the initial state shown in Figure S1. Scatterplots of: (a) Modelled versus observed ice flow speed. (b) Modelled versus observed rate of thickness change sampled where the flow speed exceeds 100 m/year, with orange line of best fit. (c) Initial ice surface elevation versus BedMachine v3 ice surface.

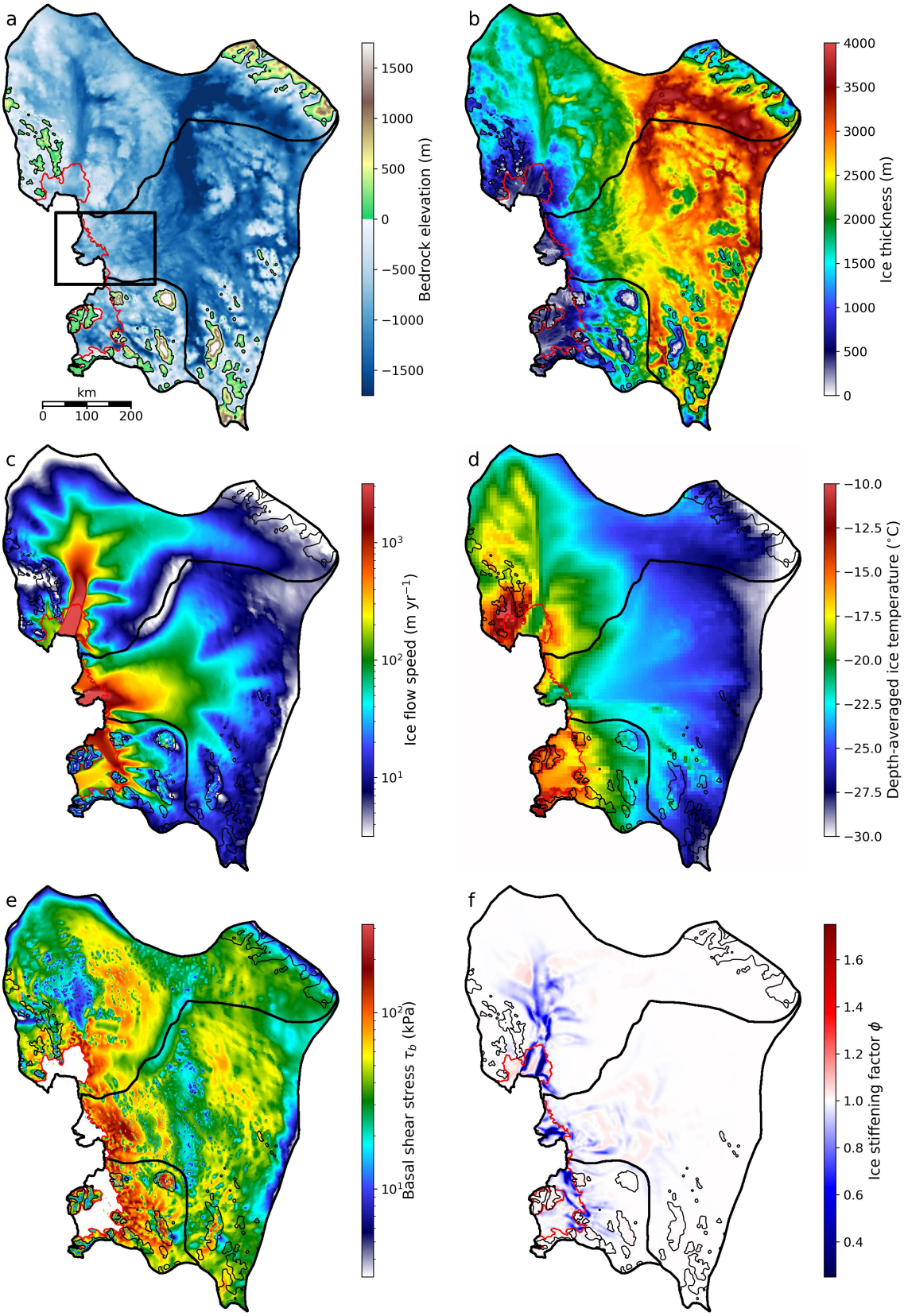

Figure S3. Model inputs following the initialization, shown only within the ASE. (a) Bed topography, (b) ice thickness, (c) modelled ice flow speed, (d) depth-averaged ice temperature, (e) basal shear stress and (f) ice stiffening factor. Thick black contours outline the drainage basins, thin black contours show the sea level contour of bed depth and red lines highlight the grounding line. The basal friction coefficient C is set to be large beyond the ASE boundary to effectively isolate the ASE. The box in (a) shows the spatial extent of other figures.

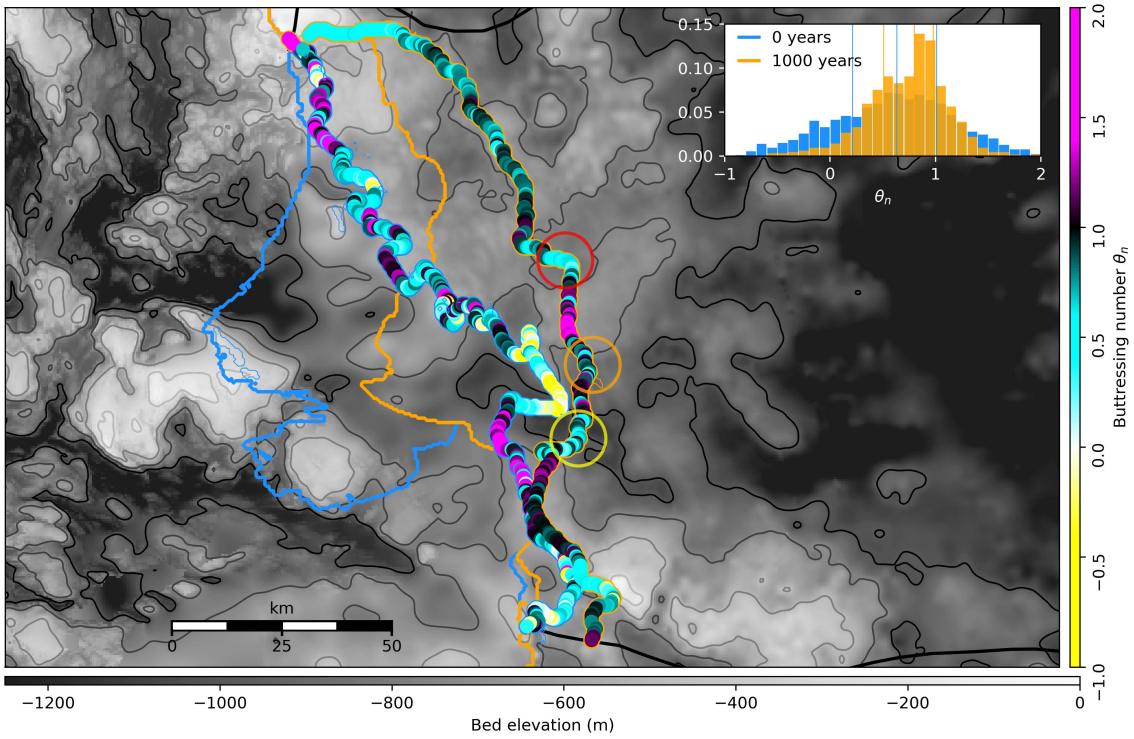

Figure S4. Buttressing numbers calculated for the TG grounding line for the initial and final states. Thick blue and orange lines mark the ice extent and thick black lines mark the TG basin boundary. Plotted buttressing factors are bordered in blue or orange to indicate the epoch. Coloured circles highlight potential vulnerabilities. The inset histogram shows grounding line buttressing numbers with quartile values highlighted by vertical lines. The extent of the zoomed in region is shown in Figure S3a. Bed contours at 250, 500, 750 and 1000 m depth are marked by grey/black contours of increasing darkness.

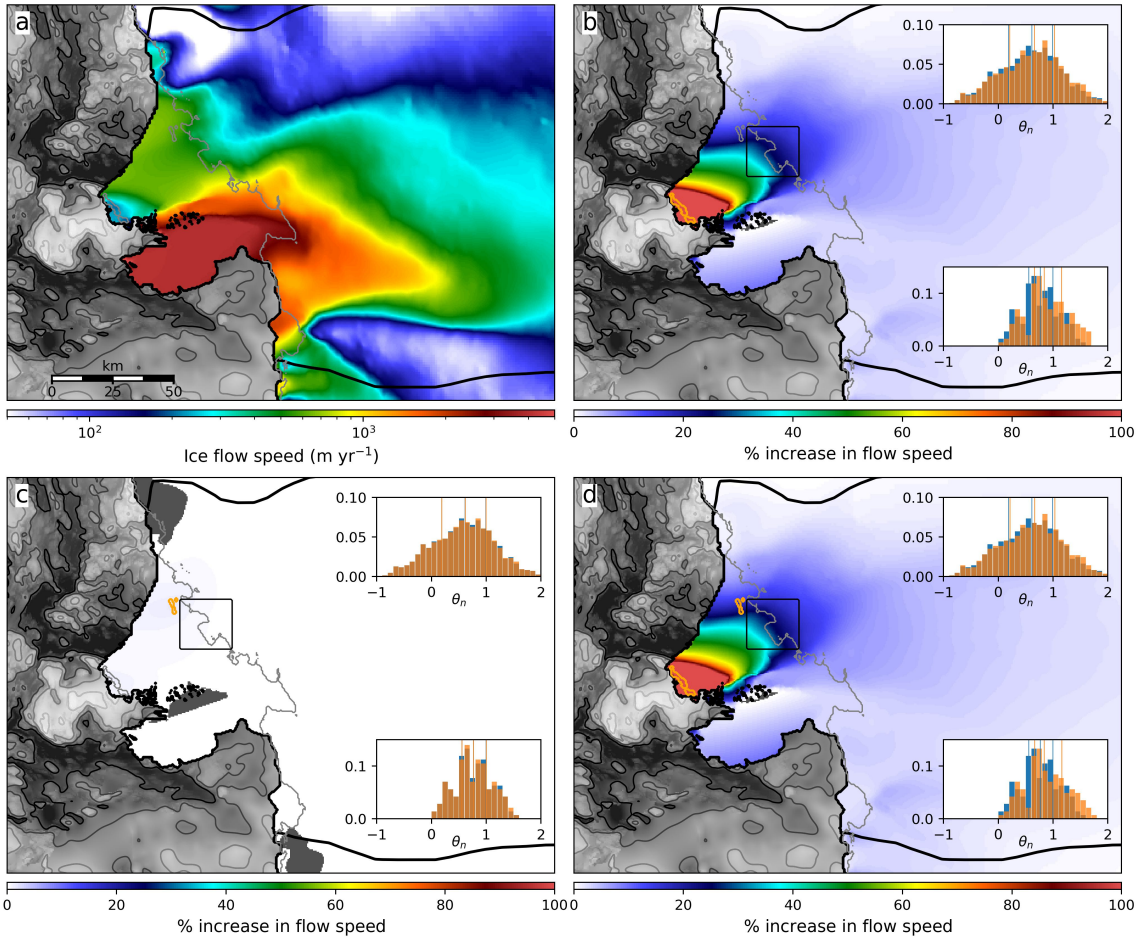

Figure S5. Impact of pinning point removal. (a) Ice flow speed for TG ice shelf and grounding line region. (b) to (d) Instantaneous percentage increase in flow speed associated with removal of the orange-highlighted pinning points. Pinning points were removed by setting the basal friction coefficient to those cells to zero. Regions that saw a slowdown are shown in grey. Inset histograms in (b) to (d) show the shift in buttressing number θ_n before (blue) and after (orange) pinning point removal. The upper histogram in each panel shows buttressing numbers calculated for all grounding lines cells (excluding pinning points) within the TG basin, while the lower histogram shows buttressing numbers calculated for the region within the black box. The extent of the zoomed in region is shown in Figure S3a. Bed maps and contours in each panel follow the same scale as in Figure S4.

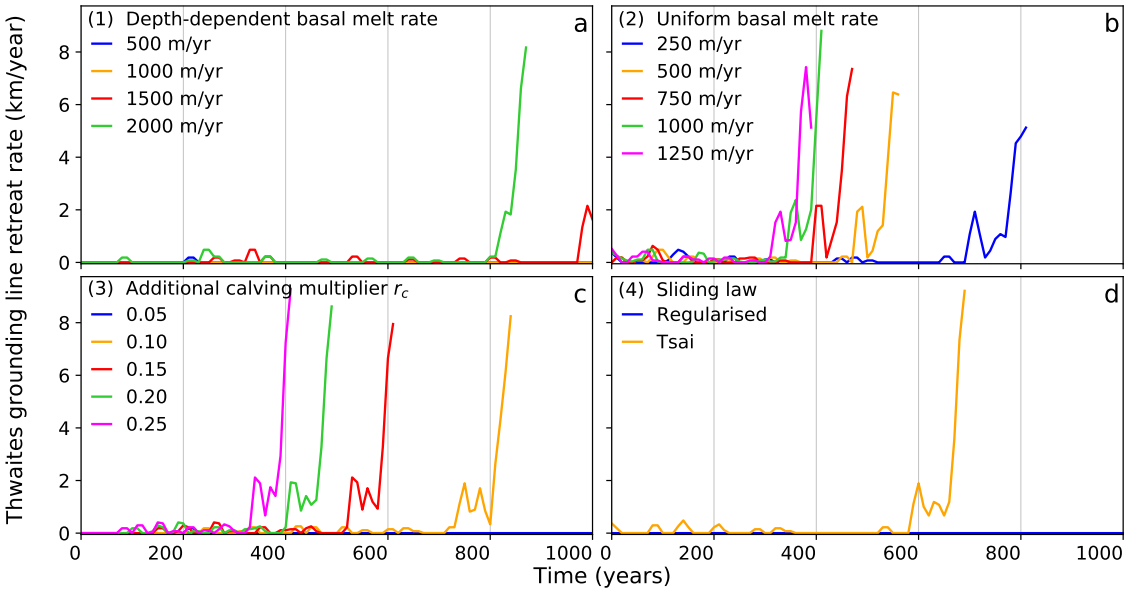

Figure S6. Grounding line retreat rates along the TG flowline for enhanced forcing experiments (see Figure 4).

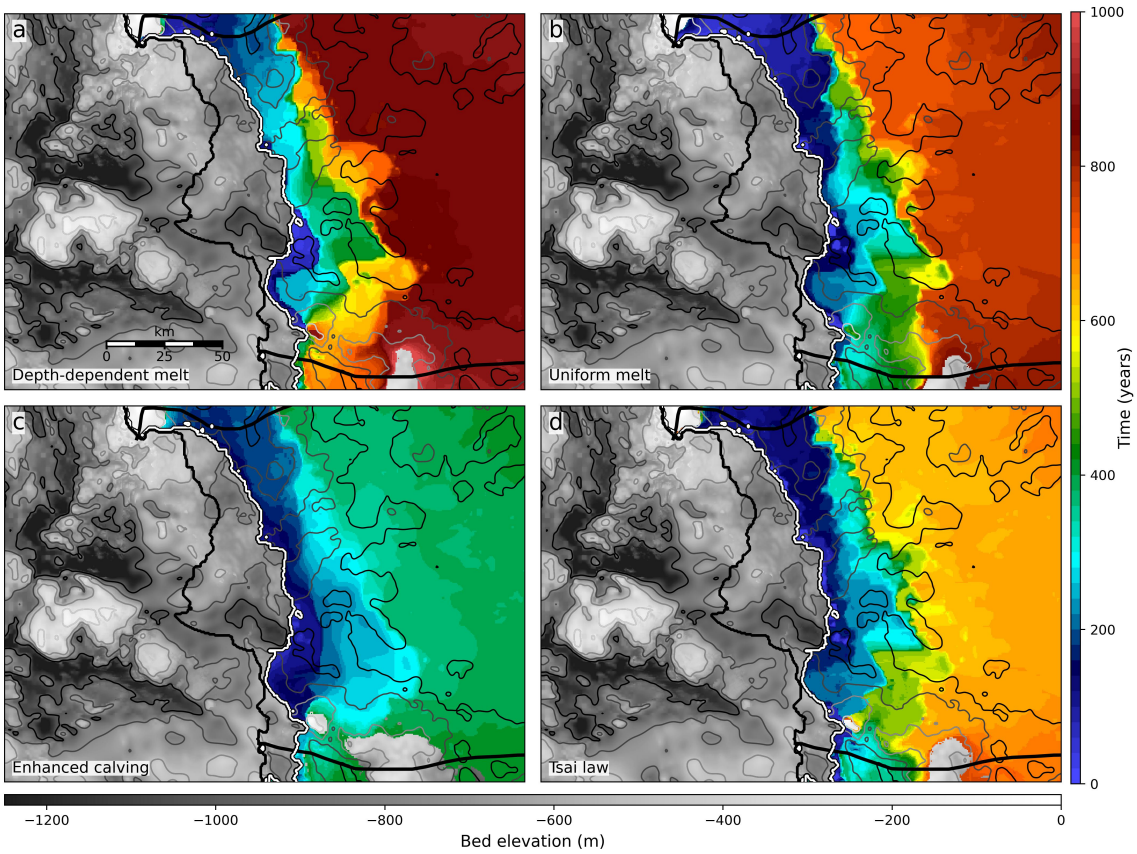

Figure S7. Time of earliest ungrounding in TG continuation experiments: (a) Depth-dependent melt rate 2000 m/yr. (b) Uniform melt rate 250 m/yr. (c) Additional calving rate with rate multiplier 1.25. (d) Tsai sliding law.The extent of the zoomed in region is shown in Figure S3a. Bed map and contours in each panel follow the same scale as in Figure S4.

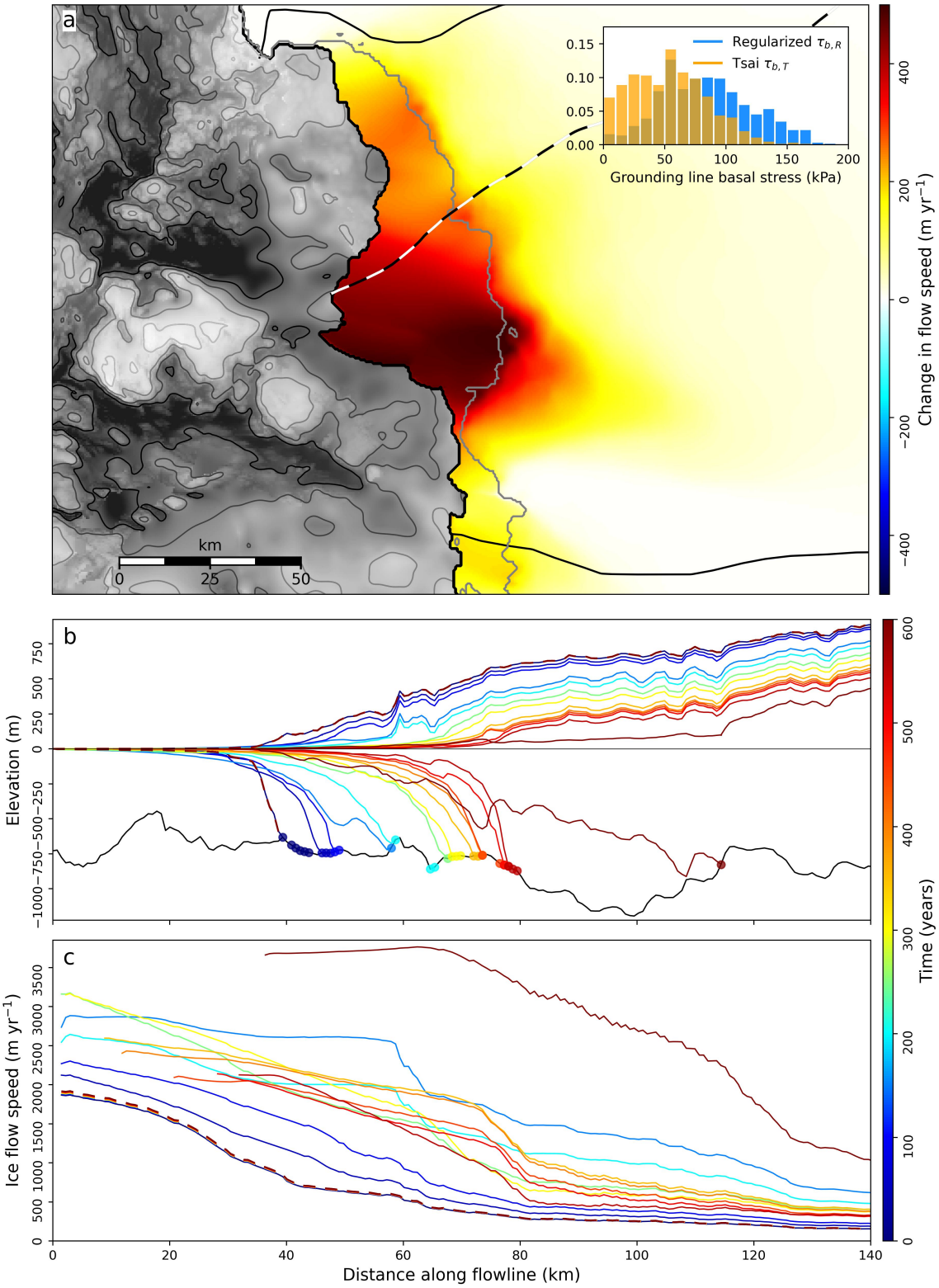

Figure S8. Comparison of Tsai and Regularised sliding law experiments (Figure 4d). (a) Instantaneous speedup when the Tsai law was applied. The inset histogram shows basal stress sampled at the grounding line for Regularised (blue) and Tsai (orange) laws. The extent of the zoomed in region is shown in Figure S3a. Bed map and contours in (a) follow the same scale as in Figure S4. (b) and (c) respectively show ice geometry and velocity along the flowline (black and white line, panel (a)) at 50-year intervals. Solid lines in (b) and (c) show the Tsai law while dashed lines show the Regularised law. Note that dashed lines overlap due to stagnation with the Regularised law. Circles plotted at the bed in (b) show where the Tsai rule determines the basal stress.

Information and Captions for Movies S1 to S8

We include animated plots of the experiments presented in Section 3.1. Movies S1 and S2 visualise the experiment groupings from Figures 2 and 3 respectively, while Movies S3 to S8 show individual experiments. Table S1 contains information on Movies S1 to S8.

Movie S1. Movie visualisation of Figure 2, showing the evolution of the ASE for PIG, TG, combined PIG and TG and full ASE melt experiments. (a) Grounding line evolution (coloured lines). Also shown are the basin boundaries and initial ice front (black lines) and initial grounding line (white lines with black edges) superimposed over the bed topography. The PIG and TG flowlines are also shown. (b) Volume above flotation (VaF) loss from the ASE. The dashed blue and orange line shows the summed VaF loss from the individual PIG and TG melt experiments. (c) Grounding line retreat along flowlines in PIG (dashed lines) and TG (solid lines). Lines are truncated where the grounding line retreats beyond the end of the flowline, shown by black horizontal lines. (d) Ice flux per unit length across the PIG-TG basin boundary, defined such that positive flux refers to flow out of the TG basin. (b) to (d) also include timesliders referencing the current time in (a).

Movie S2. Movie visualisation of Figure 3, showing the evolution of the ASE for CD, TG and combined CD and TG melt experiments. (a) to (d) as for Movie S1, except that dashed lines in (c) refer to the CD basin and fluxes in (d) are measured across the CD-TG basin boundary.

Movies S3 to S8. Movie visualisations of individual experiments. (a) to (d) as for Movies S1 and S2, except that (a) additionally shows the total thickness change. Dashed lines in (c) and fluxes in (d) refer to different basins depending on the experiment. See Table S1 for these details.

Movie	**Experiments**	**Retreat flowline**	**Basin boundary**	**Corresponding figure**
S1	PIG isolated melt TG isolated melt Combined PIG+TG melt Full ASE melt (CD+PIG+TG)	PIG	PIG-TG	Figure 2
S2	CD isolated melt TG isolated melt Combined CD+TG melt	CD	CD-TG	Figure 3
S3	PIG isolated melt	PIG	PIG-TG	Figure 2
S4	TG isolated melt	PIG	PIG-TG	Figure 2
S5	Combined PIG+TG melt	PIG	PIG-TG	Figure 2
S6	Full ASE melt (CD+PIG+TG)	PIG	PIG-TG	Figure 2
S7	CD isolated melt	CD	CD-TG	Figure 3
S8	Combined CD+TG melt	CD	CD-TG	Figure 3

Table S1. Details of Movies S1 to S8. Retreat flowlines refer to dashed lines in Panel c. Basin boundaries refer to Panel d.

References

Agosta, C., Amory, C., Kittel, C., Orsi, A., Favier, V., Gallée, H., ... Fettweis, X. (2019). Estimation of the Antarctic surface mass balance using the regional climate model MAR (1979–2015) and identification of dominant processes. *The Cryosphere*, *13*(1), 281–296. doi: 10.5194/tc-13-281-2019

Bevan, S., Cornford, S. L., Gilbert, L., Otosaka, I., Martin, D., & Surawy-Stepney, T. (2023). Amundsen Sea Embayment ice-sheet mass-loss predictions to 2050 calibrated using observations of velocity and elevation change. *Journal of Glaciology*, 1–11. doi: 10.1017/jog.2023.57

Burton-Johnson, A., Dziadek, R., & Martin, C. (2020). Review article: Geothermal heat flow in Antarctica: current and future directions. *The Cryosphere*, *14*(11), 3843–3873. doi: 10.5194/tc-14-3843-2020

Cornford, S. L., Martin, D. F., Graves, D. T., Ranken, D. F., Le Brocq, A. M., Gladstone, R. M., ... Lipscomb, W. H. (2013, jan). Adaptive mesh, finite volume modeling of marine ice sheets. *Journal of Computational Physics*, *232*(1), 529–549. doi: 10.1016/j.jcp.2012.08.037

Gudmundsson, G. H., Barnes, J. M., Goldberg, D. N., & Morlighem, M. (2023). Limited Impact of Thwaites Ice Shelf on Future Ice Loss From Antarctica. *Geophysical Research Letters*, *50*(11), 1–11. doi: 10.1029/2023gl102880

Holland, P. R., Bevan, S. L., & Luckman, A. J. (2023). Strong Ocean Melting Feedback During the Recent Retreat of Thwaites Glacier. *Geophysical Research Letters*, *50*, 1–11. doi: 10.1029/2023GL103088

Morlighem, M. (2022). *MEaSUREs BedMachine Antarctica, Version 3 [Data Set].* Retrieved 01-29-2024, from `https://nsidc.org/data/nsidc-0756/versions/3` doi: https://doi.org/10.5067/FPSU0V1MWUB6

Mouginot, J., Rignot, E., & Scheuchl, B. (2019). *MEaSUREs Phase-Based Antarctica Ice Velocity Map, Version 1 [Data Set].* Retrieved 2024-01-29, from `https://nsidc.org/data/nsidc-0754/versions/1` doi: https://doi.org/10.5067/PZ3NJ5RXRH10

Mouginot, J., Scheuchl, B., & Rignot, E. (2017). *MEaSUREs Antarctic Boundaries for IPY 2007-2009 from Satellite Radar, Version 2 [Data Set].* Retrieved 2024-01-29, from `https://nsidc.org/data/nsidc-0709/versions/2` doi: https://doi.org/10.5067/AXE4121732AD

Rignot, E., Jacobs, S., Mouginot, J., & Scheuchl, B. (2013, jul). Ice-Shelf Melting Around Antarctica. *Science*, *341*(6143), 266–270. doi: 10.1126/science.1235798

Shean, D. E., Joughin, I. R., Dutrieux, P., Smith, B. E., & Berthier, E. (2019). Ice shelf basal melt rates from a high-resolution digital elevation model (DEM) record for Pine Island Glacier, Antarctica. *The Cryosphere*, *13*(10), 2633–2656. doi: 10.5194/tc-13-2633-2019

Smith, B. E., Fricker, H. A., Gardner, A. S., Medley, B., Nilsson, J., Paolo, F. S., ... Zwally, H. J. (2020). Pervasive ice sheet mass loss reflects competing ocean and atmosphere processes. *Science*, *368*(6496), 1239–1242. doi: 10.1126/science.aaz5845

van den Akker, T., Lipscomb, W., Leguy, G., Bernales, J., Berends, C., van de Berg, W. J., & van de Wal, R. S. W. (2023). Present-day mass loss rates are a precursor for West Antarctic Ice Sheet collapse. *Research Square*, *PREPRINT (*. Retrieved from `https://www.researchsquare.com/article/rs-3498111/v1` doi: https://doi.org/10.21203/rs.3.rs-3498111/v1